Cardiac myosin-binding protein C decorates F-actin: Implications for cardiac function

Andrew E. Whitten[a,b], Cy M. Jeffries[b], Samantha P. Harris[c,1], and Jill Trewhella[b,1]

[a]Bragg Institute, Australian Nuclear Science and Technology Organisation, Lucas Heights, NSW 2234, Australia; [b]School of Molecular and Microbial Biosciences, University of Sydney, NSW 2006, Australia; and [c]Department of Neurobiology, Physiology, and Behavior, University of California, Davis, CA 95616

Edited by Clara Franzini-Armstrong, University of Pennsylvania School of Medicine, Philadelphia, PA, and approved October 9, 2008 (received for review September 8, 2008)

Cardiac myosin-binding protein C (cMyBP-C) is an accessory protein of striated muscle sarcomeres that is vital for maintaining regular heart function. Its 4 N-terminal regulatory domains, C0-C1-m-C2 (C0C2), influence actin and myosin interactions, the basic contractile proteins of muscle. Using neutron contrast variation data, we have determined that C0C2 forms a repeating assembly with filamentous actin, where the C0 and C1 domains of C0C2 attach near the DNase I-binding loop and subdomain 1 of adjacent actin monomers. Direct interactions between the N terminus of cMyBP-C and actin thereby provide a mechanism to modulate the contractile cycle by affecting the regulatory state of the thin filament and its ability to interact with myosin.

familial hypertrophic cardiomypathy | C protein | muscle regulation | neutron contrast variation | small-angle scattering

Interest in cardiac myosin-binding protein C (cMyBP-C) has been stimulated in recent times because of its influence on fine-tuning heart muscle contraction and its links to inherited cardiac disorders (1). Medical research estimates that up to 1 in 500 adolescents and young adults is affected by the diverse genetic condition known as familial hypertrophic cardiomyopathy (FHC) (2), which presents as a gradual thickening of the ventricle walls of the heart and a correlated increase in the risk of heart failure. Approximately 63% of FHC cases are attributable to mutations in genes that encode sarcomeric proteins, the majority of which (42%) are mutations in the *MYBPC3* gene (3). Of the 150 known FHC-causing mutations distributed throughout the *MYBPC3* gene, 26 are located in the region that encodes the 4 N-terminal domains of the protein.

The primary components of muscle thick and thin filaments are the proteins myosin and actin, respectively. Muscle shortens and develops force as thin filaments slide past thick filaments via the cyclic interactions of myosin cross-bridges (myosin-S1) extending from the thick filament to actin. These actomyosin interactions are regulated in part by calcium signals that are transmitted via thin-filament accessory proteins troponin and tropomyosin, whose movement on the thin filament unveils myosin-binding sites, permitting productive (weak to strong binding) cross-bridge transitions (4). Originally identified as a thick filament accessory protein, myosin-binding protein C (MyBP-C) also provides a thick-filament accessory protein, provides an additional regulatory layer to the contractile cycle, but the precise molecular mechanisms by which it influences actomyosin interactions are not understood. Belonging to the Ig/fibronectin superfamily of proteins, cMyBP-C consists of 11 sequentially ordered domains (C1, m, C2–C10, common to all isoforms), plus a cardiac specific N-terminal domain (C0) and proline/alanine-rich region that links C0 to C1. The N-terminal domains (C0-C1-m-C2 or C0C2) perform the regulatory functions by influencing myosin head interactions with actin filaments (5–7), whereas the C-terminal domains of cMyBP-C (C7–C10) play a key structural role in the sarcomere, binding to the myosin thick filament (8–11).

Biochemical evidence implicating an interaction between skeletal myosin-binding protein C and actin thin filaments was reported 30 years ago by Moos *et al.* (12), a finding supported by more recent studies that have narrowed the interactions with actin to the N-terminal regulatory domains of MyBP-C (13, 14). Based on X-ray diffraction data from intact skeletal muscle, it has been proposed that the N terminus of MyBP-C interacts with actin (15, 16). However, the functional significance of these interactions to muscle contraction is not known, and direct structural evidence of MyBP-C/actin binding has been lacking. We present here the results of small-angle scattering and neutron contrast variation studies that unequivocally show that C0C2 stabilizes actin in its filamentous state (as F-actin), decorating the filament in a highly regular arrangement. This specific binding interaction has implications for the regulation of myosin-S1 binding to actin via direct competition and through modulation of the interactions of thin-filament accessory proteins.

Results

The formation of a large molecular assembly from equimolar mixtures of C0C2 and actin was demonstrated by using small-angle X-ray scattering [supporting information (SI) Fig. S1*C*]. To determine the arrangement of actin and C0C2 within this assembly, we used small-angle neutron scattering with contrast variation. Differentiation between C0C2 and actin was achieved by isotopic labeling of C0C2 with deuterium (^{D}C0C2), which changes the neutron scattering-length density of C0C2 relative to actin. The relative contribution to the total scattering [$I(q)$] of each component was modulated by systematic variation of the solvent deuterium content (17). In solutions containing ≈40% D_2O, the scattering-length density of actin matches that of the solvent, and only ^{D}C0C2 contributes significantly to the scattering, whereas ^{D}C0C2 is solvent-matched between 90 and 100% D_2O.

Neutron contrast variation data were collected on assemblies of ^{D}C0C2 and cardiac actin in buffer conditions that support monomeric actin (G-actin buffer) (Fig. 1 and Fig. S2*A*) and on cardiac actin (alone) in buffer conditions that support formation of actin filaments (F-actin buffer) (Fig. S3). A contrast variation series was also collected on ^{D}C0C2 and skeletal actin in G-actin buffer (Fig. S4). The similarity of the contrast variation data from both ^{D}C0C2–actin assemblies, coupled with the near-

Author contributions: A.E.W., C.M.J., S.P.H., and J.T. designed research; A.E.W. and C.M.J. performed research; A.E.W. contributed new analytic tools; A.E.W. and C.M.J. analyzed data; and A.E.W., C.M.J., S.P.H., and J.T. wrote the paper.

The authors declare no conflict of interest.

This article is a PNAS Direct Submission.

[1]To whom correspondence may be addressed. E-mail: samharris@ucdavis.edu or itrewhella@usyd.edu.

This article contains supporting information online at www.pnas.org/cgi/content/full/0808903105/DCSupplemental.

www.pnas.org/cgi/doi/10.1073/pnas.0808903105

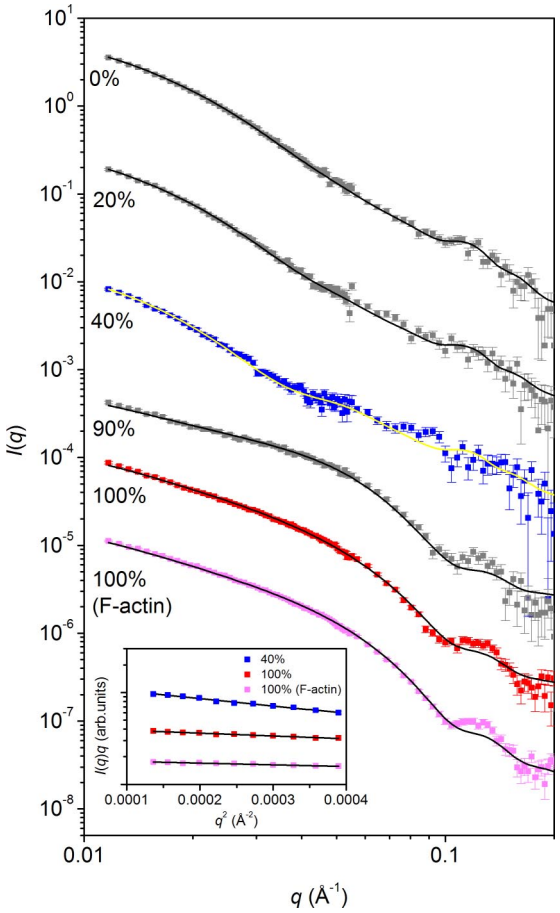

Fig. 1. Neutron scattering data with model profiles (solid lines) calculated from the final optimized 3D model of the C0C2-actin assembly. The scattering data have been placed on an absolute scale (cm^{-1}), but for clarity, 0, 20, 40, 90, 100% C0C2–actin data and 100% F-actin data have been offset by a factor of 10^{-n}, where n = 0, 1, 2, 3, 4, and 5 respectively. The χ^2 for each of the model profiles is 0.96 (0%), 1.12 (20%), 1.27 (40%), 1.34 (90%), 1.13 (100%), and 1.94 (100% F-actin). Errors shown are propagated counting statistics. (*Inset*) Guinier plot, $I(q)q$ vs. q^2, for the 40%, 100%, and 100% F-actin data.

identical amino acid sequence of the skeletal and cardiac isoforms of actin, demonstrates that the C0C2–actin assembly formation is reproducible. All of the following analyses and conclusions reached are applicable to both ^{D}C0C2–cardiac and –skeletal actin assemblies, and the structural analysis and discussion presented here will focus on data collected on the ^{D}C0C2–cardiac actin assembly.

C0C2 Stabilizes Actin Filaments in Solution. The correspondence between the scattering data measured for the ^{D}C0C2–actin assembly in 100% D_2O (close to the solvent match point of the ^{D}C0C2) and cardiac F-actin indicates that the arrangement of actin molecules in both the ^{D}C0C2–actin assembly and F-actin is similar. Specifically, the weak diffraction peak centered between q = 0.11 and 0.12 $Å^{-1}$ observed in each dataset corresponds to the well-characterized actin monomer–monomer repeat distance of ≈55 Å in actin filaments. This result is surprising, given that the experiments on the C0C2–actin assembly were performed in buffer conditions that are known to favor G-actin over F-actin (Fig. S1*B*). Thus, it appears that C0C2 plays a role in stabilizing actin filaments.

C0C2 Decorates Filamentous Actin in a Symmetric, Regular Arrangement. Information relating to the cross-sectional distribution of scattering density in the approximately rod-shaped assembly

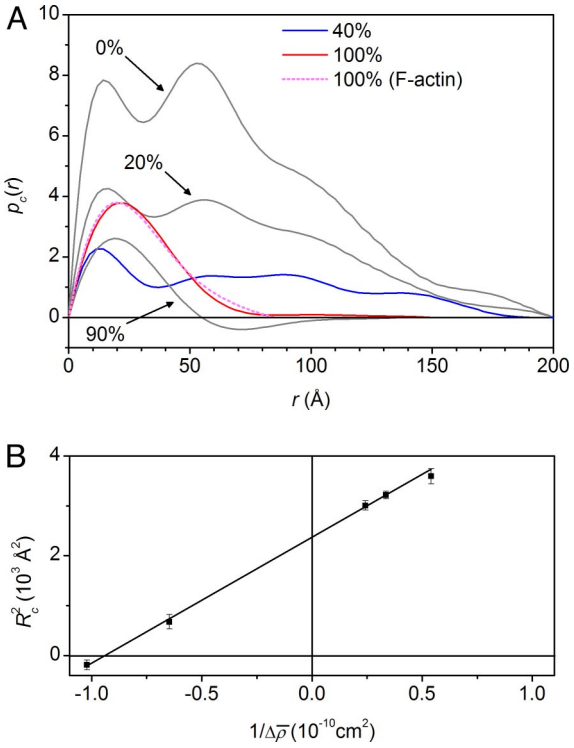

Fig. 2. Analysis of scattering data. (*A*) Pair–distance distribution profiles of cross-section [$p_c(r)$] calculated from the scattering data in Fig. 1. (*B*) Stuhrmann plot for the radius of gyration of cross-section (R_c^2).

formed by C0C2–actin was obtained by analysis of $I(q)q$ vs. q (18), where multiplication of the scattering data by q effectively removes the longitudinal structural information from the data. Guinier plots of $I(q)q$ vs. q^2 are linear (Fig. 1 *Inset*), as expected for rod-shaped particles. The absence of a decline in intensity of the Guinier plot as $q \rightarrow 0$, characteristic of the finite length of a rod-shaped scattering particle, implies that the average length of the rods is greater than the resolution limit (q_{min}) of the data.

Indirect Fourier transformation of $I(q)q$ vs. q (19) yields the pair-distance distribution functions of cross-section, $p_c(r)$ (Fig. 2*A*), the probable distribution of the contrast-weighted area elements in the scattering cross-section. From Fig. 2*A* we observe that the $p_c(r)$ profiles for the ^{D}C0C2–actin assembly close to the solvent match point for ^{D}C0C2 (100% D_2O, red), and F-actin in 100% D_2O (light magenta) are very similar in shape, with the only notable difference being the tail of the C0C2–actin profile because of imprecise matching of the ^{D}C0C2. The $p_c(r)$ profile for the ^{D}C0C2–actin assembly at the solvent match point for actin (40% D_2O, blue) extends to ≈200 Å, well beyond the length of a single C0C2 molecule (≈140 Å) (20), indicating that C0C2 molecules bind on either side of the actin filament and project away from the longitudinal axis of the filament. These structural details are consistent with the contrast dependence of the radii of gyration of cross-section R_c (Table S1), analyzed in terms of a Stuhrmann plot (21). The linear plot with positive slope shown in Fig. 2*B* signifies that ^{D}C0C2 molecules bind in an approximately symmetric arrangement and project beyond the periphery of the actin filament.

To determine the cross-sectional organization of the protein components in the ^{D}C0C2–actin assembly, we developed a 2D dummy atom modeling program, analogous to other 3D shape restoration programs (22, 23). Application of this 2D modeling program to the contrast variation data collected on the C0C2–actin assembly yields an excellent fit [average χ_w^2 = 0.80 for the assembly made with cardiac actin (Fig. 3*A*) and χ_w^2 = 0.77 for

BIOPHYSICS

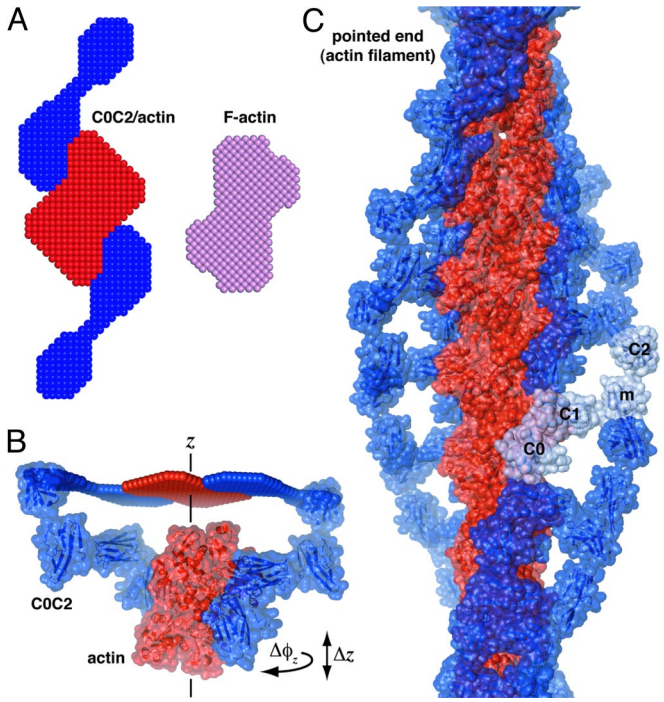

Fig. 3. Models derived from the small-angle neutron scattering data, where the actin component is shown in red, and the C0C2 component is shown is blue. (*A*) Cross-sectional dummy atom model of the C0C2–cardiac actin assembly obtained from optimization against the entire contrast variation series. The cross-sectional model for cardiac F-actin (light magenta) was obtained from optimization against the 3 contrast points measured for F-actin. The average χ_w^2 for each of the models fit to their respective scattering datasets is 0.80 (C0C2–actin) and 0.76 (F-actin) (*B*) Relationship between the cross-sectional dummy atom model and the 3D model of the complex. (*C*) Final 3D model of the C0C2–actin complex showing a central actin filament decorated regularly by C0C2 molecules (blue). The average χ^2 for the model fit to each scattering profile is 1.17.

that with skeletal actin (Fig. S4*A*); see Eq. **2** for definition of χ_w] and confirms that C0C2 molecules bind either side of the actin filament and project out into solution (Fig. 3*A*). The modeling procedure was also applied to the data collected on cardiac F-actin (χ_w^2 = 0.76; Fig. S3*A*). As expected from the $p_c(r)$ profiles (Fig. 2*A*), the cross-sectional model of F-actin and the actin component in the C0C2–actin assembly (Fig. 3*A*) are essentially the same, showing that the overall structure of F-actin is preserved in the C0C2–actin assembly.

The 3D Model of the C0C2–Actin Assembly Reveals the Actin-Binding Site. By using the arrangement of actin monomers in the F-actin model of Holmes *et al.* (24), the structure of C0C2 derived from small-angle X-ray scattering (20), and the cross-sectional model as a guide, we developed a 3D model of the ^{D}C0C2–actin assembly and optimized it against the contrast variation data. The procedure involved a grid-style rigid-body optimization of the structure of ^{D}C0C2 in the context of the repeating filamentous structure against the 40% contrast point followed by an optimization of the relationship between the ^{D}C0C2 molecules and the actin filament against the 0% contrast point (which is most sensitive to the relationship of the 2 components, see Fig. S5 *A* and *B*). There are 8 configurations of C0C2 relative to actin that possess a similar cross-sectional arrangement, and so 8 optimizations were performed, using each alternate configuration as a starting point (Fig. S5*C*).

In all cases, comparison of the model-scattering profiles with the 40% contrast point yielded $\chi^2 \approx 1.3$, which is very good given that only translational degrees of freedom of each of the domains of C0C2 were optimized. However, those models in which the m and C2 domains were placed closest to the actin filament were rejected because they showed severe interpenetration of m and C2 with the actin filament. The interpenetration observed for this class of models reflects the sensitivity of the scattering data to the differences in size and shape between C0–C1 and m–C2 domain pairs and provides evidence that the C0C2–actin binding interaction occurs via the C0–C1 end of the molecule.

For the 4 models in which the C0 and C1 domains were placed closest to the actin filament, the optimized structure of each ^{D}C0C2 molecule is largely unchanged from the determined solution structure of C0C2 alone (20); the primary difference is a change in the distance between C1 and C0 (Fig. S1*D*). Common to each of these 4 models is that C0 lies at the interface between 2 adjacent (in the longitudinal direction) actin molecules close to the DNase I-binding loop (Fig. 4*A*), C1 lies close to the actin filament near subdomain 1, and m and C2 project ≈50 Å away from the actin filament into solution. However, the

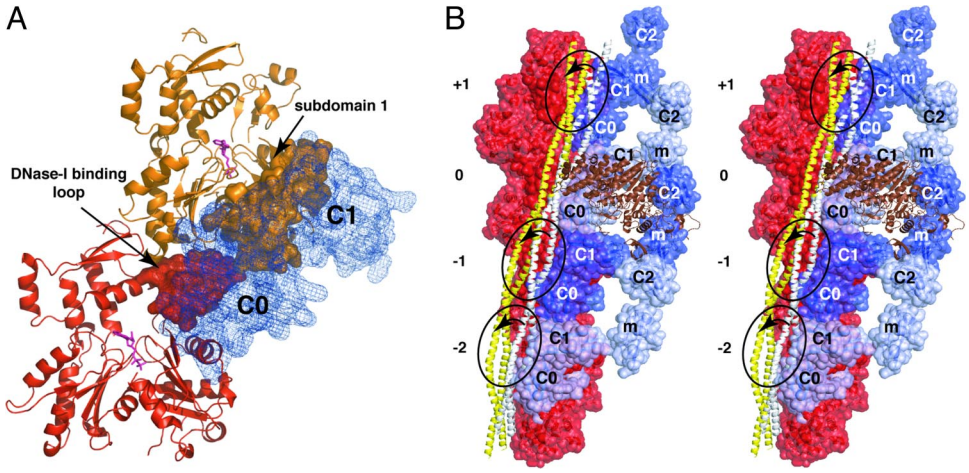

Fig. 4. Relationship among C0C2, actin, and the thin-filament accessory proteins. (*A*) Two actin molecules (red and orange) and the C0 and C1 domains (blue) of C0C2 taken from the final 3D model, highlighting the relationship between the C0 and C1 domains of C0C2 and the DNase I-binding loop (red solid surface) and subdomain 1 (orange solid surface) of actin. (*B*) Stereo image of the C0C2–actin model with the thin-filament accessory protein tropomyosin (white is the Ca^{2+} off state and yellow is the Ca^{2+} on state) and the myosin head group (brown).

quality of the fit (judged by the agreement index χ^2) for each of the model-derived scattering profiles with the 0% contrast point differs significantly. The 2 best-agreement indices among the various models are $\chi^2 = 0.96$ and 1.19, and, based on the F-test for χ^2 distributions, the likelihood that this difference is significant is >85%. We therefore present here the structure of the statistically superior model (model-scattering profiles Fig. 1; structural model Fig. 3*C*); however, the locations of the C0 and C1 domains in each of the 4 optimized models are similar, and the functional implications discussed below are the same.

Discussion

Our data show that the N-terminus of cMyBP-C decorates F-actin in a regular manner and that C0 and C1 interact with the DNase I-binding loop and subdomain 1 of neighboring actin molecules. The importance of the DNase I-binding loop in actin polymerization (25), together with the fact that C0 and C1 appear to link neighboring actin monomers, may explain the unexpected preservation of a filamentous C0C2–actin assembly in G-actin buffer conditions. Of note, the stoichiometry of the assembly results in crowding of the m and C2 domains in a configuration that runs parallel to the actin filament. In muscle sarcomeres, cMyBP-C is localized to the C zone of thick filament A bands and is only associated with every 3rd crown of myosin heads in this region (26–28). In addition, C2 is connected to domains C3–C10 of cMyBP-C, which is also anchored to the thick filament. Therefore, the positions and orientations of the m and C2 domains in this saturated C0C2–actin assembly may not be physiological, and for this reason the following discussion will focus on the C0C2–actin binding interface and the implications that this has for muscle regulatory mechanisms.

Our model suggests that cMyBP-C can influence muscle contraction via an interaction with tropomyosin and/or myosin cross-bridges and thereby influence the activation state of the thin filament (Fig. 4*B*). In fact, our C0C2–actin structure predicts significant steric clashes with tropomyosin, especially under conditions of low Ca^{2+} when tropomyosin normally occupies a position that blocks myosin cross-bridge binding to the thin filament (29, 30). If C0 and C1 displace tropomyosin away from this blocked configuration under relaxed (low Ca^{2+}) conditions, then cMyBP-C could effectively prime thin-filament activation by uncovering myosin-binding sites in the absence of Ca^{2+}. This mechanism could explain observations that C0C2 activates thin-filament motility in vitro (14). It could also explain force development in sarcomeres in low Ca^{2+} (31) and the apparent increased Ca^{2+} sensitivity of cross-bridge cycling (5, 32). The predicted overlap of binding sites for C0 and C1 and tropomyosin under low-Ca^{2+} conditions suggests that cMyBP-C may interact more strongly with the thin filament at high Ca^{2+} (33) or in the presence of strongly bound cross-bridges, i.e., when the thin filament is fully activated and cross-bridge-binding sites are completely uncovered. If C0 and C1 preferentially bind to activated thin filaments, then relaxation (after a decline in Ca^{2+}) could be slowed. Intriguingly, the position of C0 and C1 on actin is also predicted to overlap with myosin cross-bridge-binding sites, which could explain observations that the cMyBP-C and myosin-S1 compete for actin binding (12, 34).

A definitive result from our scattering experiments is the demonstration of a specific interaction between the N-terminal domains of cMyBP-C and actin, which means that the intact cMyBP-C forms a linkage between the thick and thin filaments of cardiac muscle. Thus, in addition to being positioned to influence the interactions of accessory proteins and myosin-S1 with the thin filament, cMyBP-C provides a means by which the dynamics of the thick- and thin-filament spacings could be influenced during the contractile cycle, which is critically important for healthy heart function.

Methods

Small-Angle X-Ray Scattering. Details regarding the Bruker Nanostar small-angle X-ray scattering instrument, data collection, data reduction, and analysis procedures, along with the preparation of C0C2 are described elsewhere (20). Small-angle X-ray scattering data were collected for 1 h at 23 °C on both rabbit skeletal actin at 47.6 μM (2.0 mg/mL and a mixture of C0C2 and actin (≈25 μM each, 4.4 mg/mL); each was dialyzed at 4 °C against G-actin buffer [0.2 mM $CaCl_2$, 0.2 mM ATP, with 0.5 mM DTT, 5 mM Tris (pH 8.0)]. Scattering data were collected on the dialysate for 1 h at 23 °C, which serves as a solvent blank measurement.

Expression and Purification of Deuterated C0C2. The expression plasmid encoding *Mus musculus* cMyBP-C N-terminal domain proteins C0C2 (cMyBP-C residues 1–447 coupled with an N-terminal MKHHHHHHH affinity tag) is described in ref. 14. Residue numbering is in accordance with GenBank accession no. NM_008653. ^{D}C0C2 was expressed in *Escherichia coli* Rosetta 2 cells (Invitrogen) grown in 83.3% D_2O M9 minimal medium supplemented with [^{1}H]glucose (4 g/L), ampicillin (60 μg/mL), and chloramphenicol (15 μg/mL), pH 6.5 (pD 6.1). Growth was performed at 37 °C to a cell density of $OD_{595} = 0.7$, whereupon isopropyl-β-D-thiogalactopyranoside was added to a concentration of 1 mM to induce protein expression. Cell cultures were then incubated at 15 °C for 48 h to express ^{D}C0C2. The ^{D}C0C2 was then purified as described in ref. 20 and maintained in a nondeuterated storage buffer [400 mM NaCl, 2 mM Tris[2-carboxyethyl]phosphine hydrochloride (TCEP-HCl), 50 mM Tris·HCl (pH 7.5)]. The deuteration level of ^{D}C0C2 was determined by using a comparative peptide mass fingerprinting analysis of ^{D}C0C2 against C0C2. Peptide mass shifts were analyzed by using a QSTAR XL Hybrid Mass Spectrometer (Applied Biosystems), equipped with an oMALDI source. A mass increase of 3.3% was observed for the ^{D}C0C2 peptide fragments, equating to a deuteration level for the nonexchangeable hydrogen positions of 62%.

Preparation of C0C2–Actin Complexes for Neutron Scattering. Unlabeled bovine cardiac actin and rabbit skeletal actin were obtained from Cytoskeleton, Inc. Each of the actin samples was resuspended in G-actin buffer (with 2 mM TCEP-HCl substituted for the DTT) to a final concentration of 127 μM (cardiac actin) or 141 μM (skeletal actin). ^{D}C0C2 in the specified storage buffer was added to either cardiac or skeletal actin samples in a 1:1 molar ratio to form 2 individual ^{D}C0C2–actin stock solutions (final concentrations: ^{D}C0C2–cardiac actin: 64 μM; ^{D}C0C2–skeletal actin: 64.5 μM). Aliquots of 350 μL from either the ^{D}C0C2/cardiac or skeletal actin stock solutions were individually dialyzed overnight at 4 °C against G-actin buffer containing 0, 20, 40, 90, and 100% vol/vol D_2O. In a separate experiment, cardiac actin was made to a final concentration of 64.2 μM in G-actin buffer, and 350-μL aliquots were dialyzed overnight at 4 °C against high salt F-actin buffer containing 0, 90 and 100% vol/vol D_2O [F-actin buffer: 50 mM KCl, 2 mM $MgCl_2$, 0.2 mM $CaCl_2$, 2 mM TCEP-HCl, 1 mM ATP, 5 mM Tris (pH 8.0)]. Protein concentrations of ^{D}C0C2 and cardiac and skeletal actin solutions were determined at A_{280} nm by using the following: 7His-C0C2, ε = 60,500 L·mol^{-1} cm^{-1} (M_r, 49,900 g·mol^{-1}); cardiac actin, ε = 38,200 L·mol^{-1} cm^{-1} (M_r, 42,020 g·mol^{-1}); skeletal actin, ε = 38,300 L·mol^{-1} cm^{-1} (M_r, 42,050 g·mol^{-1}). All samples were preequilibrated to 23 °C before analysis.

Small-Angle Neutron Scattering Data Collection. Small-angle neutron scattering data were collected on the NG3 30 m SANS instrument at the National Institute for Standards and Technology (NIST) Center for Neutron Research (NCNR) (35) by using a neutron wavelength λ = 6.0 Å ($\Delta\lambda/\lambda$ = 0.142) and sample to detector distances of 1.33 m (detector offset by 0.25 m, q-range 0.030–0.467 Å^{-1}) and 6.5 m (detector centered, q-range 0.008–0.071 Å^{-1}). Data collection times were 60 min for the 6.5 m configuration and 30 min for the 1.33 m configuration. Samples were maintained at 23 °C during the course of data acquisition. Data reduction to $I(q)$ vs. q used the procedures described elsewhere (36, 37).

Small-Angle Neutron Scattering Data Analysis. *Two-dimensinal analysis.* Indirect Fourier transformation of small-angle scattering data [$I(q)q$ vs. q] was performed by using GNOM (38), accounting for beam shape and wavelength distribution. In all cases, data $q < 0.10$ Å^{-1} were used to prevent any bias caused by the small peak centered between q = 0.11 and 0.12 Å^{-1}. This peak arises from small, regular variations from a perfect cylindrical shape along the length of the filament and cannot be separated from the transverse contribution to the scattering. The transformation yielded the probable distribution of distances between area elements of cross-section, weighted by the contrast of each area element [$p_c(r)$]. From $p_c(r)$, the zero-angle scattering of cross-section [I_c (0) related to the mass per unit length of the filament] (39), radius

of gyration of cross-section (R_c) and maximum cross-sectional dimension (D_c) were determined.

Two-dimensional modeling. The scattering data were analyzed in terms of a 2-phase dummy atom model of the average cross-section of the filament, which was corefined against the neutron contrast variation data, assuming C_2 symmetry. The initial dummy atom model was composed of randomly distributed atoms types (actin, C0C2, or solvent), each 3 Å in size, arranged in a grid with dimensions of 32 × 64. This model was optimized by using a simulated annealing algorithm implemented in a purpose written program, analogous to that written by Svergun and colleagues for 3-dimensional shape restoration (22, 23), with some differences. The procedure of Svergun and colleagues uses a multipole expansion to describe the $\Delta\rho(\mathbf{r})$ distribution, which is readily and efficiently transformed into scattering amplitudes. However, because the implementation of their method is not straightforward and because the 2D model refined here contains a relatively small number of dummy atoms compared with a 3D model, it is not computationally prohibitive to evaluate of the pair–distance distribution function of cross-section of the $\Delta\rho(\mathbf{r})$ distribution [p_c (r)] and calculate the scattering profile of a filament via the relationship,

$$I_1(q) = (2\pi^2/q)\int_0^{D_{max}} p_c(r)J_0(qr)dr. \qquad [1]$$

Corrections for instrumental smearing, scaling, and incoherent background are readily applied for comparison of the model profile with the measured scattering data. Accounting for these effects, the expression minimized during the optimization was

$$\varepsilon = \frac{1}{N_{CP}N_P}\sum_i^{N_{CP}}\sum_j^{N_P}\left(\frac{I^i(q_j) - m^i\int_0^\infty I_1^i(q)R(q,\bar{q}_j)dq + b^i}{w\sigma(I^i(q_j))}\right)^2 + \frac{(C_{loose} + C_{connect})}{10},$$

$$= {\chi_w}^2 + Restraints \qquad [2]$$

where N_{CP} is the number of contrast points; N_P is the number of data points at each contrast point; m^i and b^i are the scale and incoherent background corrections at each contrast point, respectively; $R(q,\bar{q}_j)$ is the resolution function for point q_j (40); C_{loose} and $C_{connect}$ are looseness and connectivity restraints, which are the same as those defined by Svergun and Nierhaus (22, 23), except the number of nearest neighbors for each dummy atom is 8 instead of 12. The weighting factor $w = 1 + 3 \times \exp[-(0.114 - q_j)^2]/0.00024$ was used to down-weight the contribution of data points in the scattering profiles affected by nonuniformity of the cross-section of the filament. The need for this weighting term stems from the assumption in Eq. **1** of a homogeneous distribution of scattering density along the length of the filament. The exponential term in the weighting function is a Gaussian centered on $q = 0.114$ Å^{-1}, with a standard deviation of $\sigma = 0.011$ Å^{-1} (related to the width of the diffraction peak). The weighting factor w effectively down-weights data points at $q = 0.114$ Å^{-1} by a factor of 4, dropping off to essentially 1 at $q < 0.08$ Å^{-1} and $q > 0.15$ Å^{-1}, preventing any significant bias caused by the diffraction peak. The optimization procedure was repeated ≈20 times, yielding very similar models in each case, indicating that the model is unique.

Three-dimensional modeling. Developing a 3D model involved 3 steps: (*i*) building the actin filament, (*ii*) adding C0C2 to the filament and optimizing the positions of the domains within C0C2 against the 40% contrast point (where the scattering is dominated by ^{D}C0C2), then (*iii*) optimizing the relationship between C0C2 and actin against the 0% contrast point, which is most sensitive to this information.

Building the actin filament. The nth molecule in the F-actin filament was generated by applying a −167.13 n° rotation around the z-axis, and a 27.5 nÅ translation along the z-axis, to an actin monomer taken from Holmes *et al.* (24). The scattering profiles of actin filaments of various lengths were calculated to $q_{max} = 0.20$, by using CRYSON (41) with an appropriate order for the multipole expansion ($L_{max} > \pi D_{max}q_{max}/12$). The shape of scattering profiles between $q = 0.01$ and 0.20 Å^{-1} were found to be essentially unchanged above $n_{max} = 30$ (corresponding to a filament length of ≈850 Å); hence, at the resolution of the experiment, the scattering profiles generated from filaments with $n_{max} = 30$ are a good approximation for an ensemble of long rods.

Optimizing the C0C2 domain positions. The initial C0C2 structure was taken from previous studies (20) and docked onto an actin monomer in various starting orientations, such that its projection onto the xy plane was consistent with the 2D dummy atom model (Fig. 3*B*). This structure was then transformed into a filament in exactly the same manner used to generate the F-actin filament. Each structure was then subjected to an iterative optimization of the positions of the domains in C0C2 against the 40% contrast point, where the scattering is dominated by ^{D}C0C2 (outlined in the flowchart Fig. S6). Manual optimization including rotational degrees of freedom is not feasible, and because the domains are all globular any resulting bias in the positions of the domains should be small.

Optimizing the position and orientation of C0C2 with respect to the actin filament. The relative orientations of the actin and C0C2 were refined manually against the scattering data from the 0% contrast point, which encodes the most information regarding the relative orientation of C0C2 and actin. A systematic approach was adopted because there are only 2 variables that leave the relationship of the C0C2 molecules with respect to each other unchanged: a rotation around z ($\Delta\phi_z$) and a translation along z (Δz). The optimization procedure involved determination of χ^2 as a function of both $\Delta\phi_z$ and Δz to find the global minimum in χ^2 (outlined in the flowchart Fig. S7).

ACKNOWLEDGMENTS. We thank Ben Crossett for performing mass spectrometry using the Australian Proteome Analysis Facility established under the Australian Government's Major National Facilities program. This work was supported by Australian Research Council Federation Fellowship FF0457488 and U.S. Department of Energy Grant DE-FG02-05ER64026 (to J.T.) and National Institutes of Health Grant HL080367 (to S.P.H.). We used facilities supported by National Science Foundation Grant DMR-0454672. We acknowledge the support of the National Institute of Standards and Technology, U.S. Department of Commerce, in providing the neutron research facilities used in this work and Boualem Hammouda for assistance in using these facilities. We also acknowledge financial support from the Australian government's Access to Major Research Facilities Program (06/07-N-27) and access to X-ray scattering instrumentation facilitated by Australian Institute of Nuclear Science and Engineering Grant AINGRA06257.

1. Flashman E, Redwood C, Moolman-Smook J, Watkins H (2004) Cardiac myosin-binding protein C: Its role in physiology and disease. *Circ Res* 94:1279–1289.
2. Maron BJ, *et al.* (1995) Prevalence of hypertrophic cardiomyopathy in a general population of young adults: Echocardiographic analysis of 4111 subjects in the CARDIA Study. *Circulation* 92:785–789.
3. Richard P, *et al.* (2003) Hypertrophic cardiomyopathy: Distribution of disease genes, spectrum of mutations, and implications for a molecular diagnosis strategy. *Circulation* 107:2227–2232.
4. Gordon AM, Homsher E, Regnier M (2000) Regulation of contraction in striated muscle. *Physiol Rev* 80:853–924.
5. Kunst G, *et al.* (2000) Myosin-binding protein C, a phosphorylation-dependent force regulator in muscle that controls the attachment of myosin heads by its interaction with myosin S2. *Circ Res* 86:51–58.
6. Weisberg A, Winegrad S (1996) Alteration of myosin cross-bridges by phosphorylation of myosin-binding protein C in cardiac muscle. *Proc Natl Acad Sci USA* 93:8999–9003.
7. Colson BA, Bekyarova T, Fitzsimons DP, Irving TC, Moss RL (2007) Radial displacement of myosin cross-bridges in mouse myocardium due to ablation of myosin-binding protein C. *J Mol Biol* 367:36–41.
8. Winegrad S (1999) Cardiac myosin-binding protein C. *Circ Res* 84:1117–1126.
9. Freiburg A, Gautel M (1996) A molecular map of the interactions between titin and myosin-binding protein C: Implications for sarcomeric assembly in familial hypertrophic cardiomyopathy. *Eur J Biochem* 235:317–323.
10. Flashman E, Watkins H, Redwood C (2007) Localization of the binding site of the C-terminal domain of cardiac myosin-binding protein C on the myosin rod. *Biochem J* 401:97–102.
11. Okagaki T, *et al.* (1993) The major myosin-binding domain of skeletal muscle MyBP-C (C-protein) resides in the COOH-terminal, immunoglobulin C2 motif. *J Cell Biol* 123:619–626.
12. Moos C, Mason CM, Besterman JM, Feng IN, Dubin JH (1978) The binding of skeletal muscle C-protein to F-actin and its relation to the interaction of actin with myosin subfragment 1. *J Mol Biol* 124:571–586.
13. Kulikovskaya I, McClellan G, Flavigny J, Carrier L, Winegrad S (2003) Effect of MyBP-C binding to actin on contractility in heart muscle. *J Gen Physiol* 122:761–774.
14. Razumova MV, *et al.* (2006) Effects of the N-terminal domains of myosin-binding protein C in an in vitro motility assay: Evidence for long-lived cross-bridges. *J Biol Chem* 281:35846–35854.
15. Squire JM, Luther PK, Knupp C (2003) Structural evidence for the interaction of C-protein (MyBP-C) with actin and sequence identification of a possible actin-binding domain. *J Mol Biol* 331:713–724.

16. Squire JM, Roessle M, Knupp C (2004) New X-ray diffraction observations on vertebrate muscle: Organisation of C-protein (MyBP-C) and troponin and evidence for unknown structures in the vertebrate A-band. *J Mol Biol* 343:1345–1363.
17. Timmins PA, Zaccai G (1988) Low-resolution structures of biological complexes studied by neutron scattering. *Eur Biophys J* 15:257–268.
18. Porod G (1982) in *Small Angle X-Ray Scattering*, eds Glatter O, Kratky O (Academic, London), pp 17–51.
19. Glatter O (1980) Evaluation of small-angle scattering data from lamellar and cylindrical particles by the indirect transformation method. *J Appl Crystallogr* 13:577–584.
20. Jeffries CM, Whitten AE, Harris SP, Trewhella J (2008) Small-angle X-ray scattering reveals the N-terminal domain organization of cardiac myosin-binding protein C. *J Mol Biol* 377:1186–1199.
21. Ibel K, Stuhrmann HB (1975) Comparison of neutron and x-ray scattering of dilute myoglobin solutions. *J Mol Biol* 93:255–265.
22. Svergun DI (1999) Restoring low-resolution structure of biological macromolecules from solution scattering using simulated annealing. *Biophys J* 76:2879–2886.
23. Svergun DI, Nierhaus KH (2000) A map of protein-rRNA distribution in the 70S *Escherichia coli* ribosome. *J Biol Chem* 275:14432–14439.
24. Holmes KC, Angert I, Kull FJ, Jahn W, Schroder RR (2003) Electron cryomicroscopy shows how strong binding of myosin to actin releases nucleotide. *Nature* 425:423–427.
25. Wawro B, Khaitlina SY, Galinska-Rakoczy A, Strzelecka-Golaszewska H (2005) Role of actin DNase-I-binding loop in myosin subfragment 1-induced polymerization of G-actin: Implications for the mechanism of polymerization. *Biophys J* 88:2883–2896.
26. Bennett P, Craig R, Starr R, Offer G (1986) The ultrastructural location of C-protein, X-protein, and H-protein in rabbit muscle. *J Muscle Res Cell Motil* 7:550–567.
27. Craig R, Offer G (1976) Location of C-protein in rabbit skeletal muscle. *Proc R Soc London Ser B* 192:451–461.
28. Zoghbi ME, Woodhead JL, Moss RL, Craig R (2008) Three-dimensional structure of vertebrate cardiac muscle myosin filaments. *Proc Natl Acad Sci USA* 105:2386–2390.
29. Pirani A, *et al.* (2006) An atomic model of the thin filament in the relaxed and Ca^{2+}-activated states. *J Mol Biol* 357:707–717.
30. Lehman W, Craig R, Vibert P (1994) The Ca^{2+}-induced tropomyosin movement in *Limulus* thin filaments revealed by 3-dimensional reconstruction. *Nature* 368:65–67.
31. Herron TJ, *et al.* (2006) Activation of myocardial contraction by the N-terminal domains of myosin-binding protein C. *Circ Res* 98:1290–1298.
32. Harris SP, Rostkova E, Gautel M, Moss RL (2004) Binding of myosin-binding protein C to myosin subfragment S2 affects contractility independent of a tether mechanism. *Circ Res* 95:930–936.
33. Moos C (1981) Fluorescence microscope study of the binding of added C-protein to skeletal muscle myofibrils. *J Cell Biol* 90:25–31.
34. Saber W, Begin KJ, Warshaw DM, Vanburen P (2008) Cardiac myosin-binding protein C modulates actomyosin binding and kinetics in the in vitro motility assay. *J Mol Cell Cardiol* 44:1053–1061.
35. Glinka CJ, *et al.* (1998) The 30 m small-angle neutron scattering instruments at the National Institute of Standards and Technology. *J Appl Crystallogr* 31:430–445.
36. Kline SR (2006) Reduction and analysis of SANS and USANS data using IGOR Pro. *J Appl Crystallogr* 39:895–900.
37. Whitten AE, *et al.* (2007) The structure of the KinA–Sda complex suggests an allosteric mechanism of histidine kinase inhibition. *J Mol Biol* 368:407–420.
38. Svergun DI (1992) Determination of the regularization parameter in indirect-transform methods using perceptual criteria. *J Appl Crystallogr* 25:495–503.
39. Orthaber D, Bergmann A, Glatter O (2000) SAXS experiments on absolute scale with Kratky systems using water as a secondary standard. *J Appl Crystallogr* 33:218–225.
40. Barker JG, Pedersen JS (1995) Instrumental smearing effects in radially symmetric small-angle neutron scattering by numerical and analytical methods. *J Appl Crystallogr* 28:105–114.
41. Svergun DI, *et al.* (1998) Protein hydration in solution: Experimental observation by X-ray and neutron scattering. *Proc Natl Acad Sci USA* 95:2267–2272.